Article

Simultaneous interneuron labeling reveals cell type-specific, population-level interactions in cortex

Simultaneous 2-photon imaging of labeled cell types

Local network state linked to ratio of mean SOM and PV activity

Christian T. Potter,
Constanza D.
Bassi, Caroline A.
Runyan

runyan@pitt.edu

Highlights

A method to distinguish multiple fluorophores *in vivo* using excitation spectra

In vivo imaging of somatostatin, parvalbumin, and the full neural population

Somatostatin and parvalbumin populations can be active together or separately

Somatostatin and parvalbumin activity events align with different population activity states
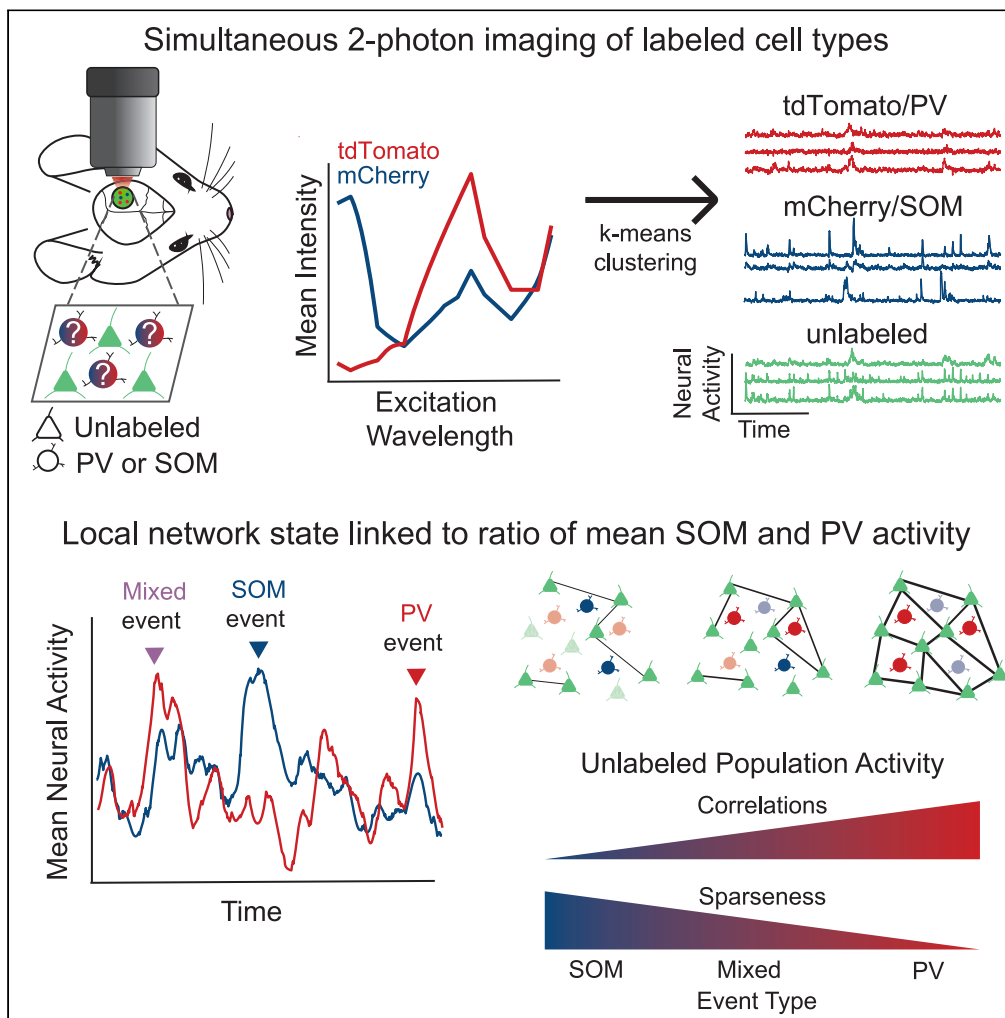
Article

Simultaneous interneuron labeling reveals cell type-specific, population-level interactions in cortex

Christian T. Potter,[1,2,3] Constanza D. Bassi,[1,2,3] and Caroline A. Runyan[1,2,4,*]

SUMMARY

Cortical interneurons shape network activity in cell type-specific ways, and interact with other cell types. These interactions are understudied, as current methods typically restrict *in vivo* labeling to one neuron type. Although post-hoc identification of many cell types has been accomplished, the method is not available to many labs. We present a method to distinguish two red fluorophores *in vivo*, allowing imaging of activity in somatostatin (SOM), parvalbumin (PV), and the rest of the neural population in mouse cortex. We compared population events in PV and SOM neurons and observed that local network states reflected the ratio of SOM to PV neuron activity, demonstrating the importance of simultaneous labeling to explain dynamics. Activity became sparser and less correlated when the ratio between SOM and PV activity was high. Our simple method can be flexibly applied to study interactions among any combination of distinct cell type populations across brain areas.

INTRODUCTION

The spatiotemporal dynamics across thousands of excitatory and inhibitory synapses dictate how a neuron responds to a propagating signal.[1] Inhibitory interneurons (INs) can therefore have profound consequences on their local network, their activity altering spiking responses of individual neurons[2] as well as network-level interactions across large populations of neurons.[3] The nature of these effects depends on an IN's cell type, which is determined by its morphology, cellular connectivity, molecular expression, and firing properties.[3] A useful classification of interneuron subtypes is based on expression of parvalbumin (PV), somatostatin (SOM), or vasointestinal peptide (VIP), which divides interneurons into three non-overlapping groups. Although these are not homogeneous cell classes, neurons within them share many key functional properties, and the three types comprise almost all cortical interneurons.[4]

Of these three types, PV and SOM neurons most strongly inhibit pyramidal cells. PV neurons are preferentially targeted by feedforward excitatory inputs from outside the network, in parallel to pyramidal neurons that they also inhibit,[5,6] controlling their response gain.[7,8] SOM neurons more broadly integrate excitation from the local population,[9] and are more sensitive to modulatory input from other regions compared to PV.[10,11] The nature of these cells' outputs is as distinct as their input patterns: PV neurons reduce activity by powerfully inhibiting the cell body, while SOM neurons inhibit the distal dendritic arbor, shaping how inputs are integrated by pyramidal neurons.[4,12] SOM neurons additionally inhibit PV neurons,[13] meaning that their activity can shift the mode of inhibition a pyramidal neuron receives. Experimental and computational work has suggested that this shift in activity corresponds to differences in cortical coding: changing the dynamic range of input a neuron receives,[12] and causing activity to become sparser[14] or less variable from trial to trial.[2] To study the interplay between PV and SOM neurons, and the impacts of their dynamics on the local population, these neurons need to be simultaneously monitored.

To characterize the function of specific cell classes using fluorescence microscopy, experimenters often non-specifically express a green calcium indicator in all neurons and use genetic tools, such as Cre/lox recombination to selectively express a red fluorophore in one cell type of interest.[15–18] This approach is thus limited to monitoring the activity of one labeled cell type along with other neurons in the population, and does not allow the observation of interactions between specific cell types and the broader activity of the population. As a result, the ability to study dynamics on individual trials is limited. A more powerful approach would allow the simultaneous recording of multiple cell types. Tools do exist to molecularly classify many cell types in tissue slices after *in vivo* imaging has been completed, but this process involves perfusing the animal, slicing the brain, staining for cell-type specific proteins, and registering the stained tissue to the *in vivo* images.[19–22] Although an established method, it is a technically challenging process that is not accessible to most labs.

To test the idea that the relative level of PV and SOM neuron activity corresponds to distinct population activity regimes, we used Cre- and Flp-dependent recombination to express distinguishable red fluorophores in PV and SOM neurons in the same mice. We exploited the

[1]Department of Neuroscience, University of Pittsburgh, Pittsburgh, PA 15213, USA
[2]Center for the Neural Basis of Cognition, University of Pittsburgh, Pittsburgh, PA 15213, USA
[3]These authors contributed equally
[4]Lead contact
*Correspondence: runyan@pitt.edu
https://doi.org/10.1016/j.isci.2024.110736

differing two-photon excitation spectra of tdTomato and mCherry,[23] discriminating PV/tdTomato and SOM/mCherry neurons from each other by their relative fluorescence intensity across a range of excitation wavelengths from 780 to 1100 nm. This allowed us to identify the two cell types using red wavelength emission, freeing the green emission channel to measure GCaMP fluorescence changes, monitoring the activity of the full neuronal population. We observed highly separable population activity events characterized by bursts in activity of one neuron type but not the other. PV events corresponded to greater levels of shared variability across more densely active unlabeled neurons, which were largely comprised of excitatory pyramidal neurons. SOM events corresponded to sparser, decorrelated activity across the unlabeled neural population. Our method, which can be applied with any standard two-photon microscope with a tunable laser and two detection channels, has revealed how specific interactions between cell types affect the broader neural population, which would not have been possible if labeling only one cell type per animal.

RESULTS

mCherry and tdTomato can be reliably identified by differences in their excitation spectra

TdTomato and mCherry are red fluorophores that are not easily distinguished by their emission spectra. However, their two-photon excitation spectra differ markedly, so in principle mCherry and tdTomato-expressing neurons could be distinguished by comparing their fluorescence intensity across excitation wavelengths.[23] To test for this possibility in vivo, we injected a Cre-dependent tdTomato construct (AAV1-pCAG-FLEX-tdTomato-WPRE) and a Flp-dependent mCherry construct (AAV1-Ef1a-fDIO-mCherry) in adjacent, but physically separate, locations in layer 2/3 of the posterior parietal cortex (PPC) of SOM-Flp (+/−) x PV-Cre (+/−) mice (Figure 1A). Next, we imaged the two sites within the same field of view in vivo across a range of excitation wavelengths. Even by eye, mCherry and tdTomato were distinguishable at different wavelengths, as the mCherry but not tdTomato site was visible at 800 nm excitation, but both were visible at 980 nm (Figures 1B and S1). We took the mean intensity of the pixels in each red cell body's region of interest (ROI) at evenly spaced wavelengths every 20 nm from 780 to 1100 nm (excluding 1020 and 1060 nm, see STAR methods), revealing separable excitation spectra between the neurons in the adjacent regions (Figures 1B and 1C).

To sort the ROIs into tdTomato+ and mCherry+ groups, we used k-means clustering for classification, as it is a simple algorithm that allowed us to specify two clusters for our data and quantify the separability of classification for each ROI (Figure 1D). Given that the separability of the two fluorophores varied across excitation wavelengths (Figures 1C and 1D), we hypothesized that a small subset of ideal excitation wavelengths would separate the ROIs more accurately than using all data. By determining which wavelengths produced the most separable clusters, we could reduce the number of neurons that would have to be excluded from analysis due to poor clustering performance. To find the highest performing excitation wavelength subsets, we performed k-means clustering on every possible combination of wavelengths and recorded the separability of each ROI, which is proportional to the confidence in classification. ROI separability was quantified by computing the silhouette score (SS), which is equal to the distance to the centroid of its assigned cluster subtracted from the distance to the other cluster's centroid (Figures S2A and 1D). The mean SS of all ROIs for each combination was strongly related to classification performance, and most combinations of wavelengths achieved >95% classification accuracy (Figures S2B and S2C). To optimize classification performance before applying it to data with intermixed mCherry and tdTomato expression, where the data could become noisier due to neuropil contamination, we ranked the combinations of wavelengths by mean SS (Figure S2D). This revealed certain wavelength combinations that produced more separable clusters. Unsurprisingly, these combinations tended to include wavelengths with greater differences in fluorescence intensity in the tdTomato- and mCherry-expression sites (Figures 1C, 1E, and 1F).

To define a threshold for cluster separation in each individual neuron, we examined the distribution of silhouette scores (SSs) from incorrectly classified neurons using "suboptimal" wavelength combinations, the combinations that included excitation wavelengths with more similar fluorescence intensity in mCherry and tdTomato sites. This allowed us to simulate clustering on noisy data (Figure S2E). We chose a conservative exclusion threshold for the SS of each neuron such that 98% of misclassified neurons would be excluded from analysis, even in this unrealistically noisy data where mCherry and tdTomato were more poorly separated overall. Comparison to SSs from clustering on our intermixed expression sites (0.93 ± 0.13, mean ± s.d.) demonstrates how much noisier our simulated data were (0.85 ± 0.20, $p = 7.64 *$ 10^{-111}, Wilcoxon rank-sum), and still this conservative estimate resulted in the exclusion of only 6.7% of neurons in intermingled data in PPC (Figure S2F). Having performed this control analysis, we could be confident that our labeling approach would rarely yield misclassified neurons after excluding neurons with worse cluster separation.

Simultaneous imaging of SOM, PV, and other neurons in layer 2/3 to study population-level interactions across cell types

Having validated our method for spectral separation of mCherry and tdTomato in vivo using physically separated control expression sites (Figure 1), we applied our approach to identify intermingled somatostatin-expressing neurons that were mCherry+ (SOM), PV neurons that were tdTomato+ (PV), and remaining unlabeled (UNL) neurons that were negative for both red fluorophores in layer 2/3 of PPC. Given that interneurons comprise only ~10–15% of neurons in the rodent cortex, and SOM and PV neurons make up ~70% of these, we would expect ~95% of the remaining neurons to be pyramidal.[4] All three neuron types expressed GCaMP6f, a genetically encoded calcium indicator to monitor and relate their ongoing spike-related activity[24] (7 mice, 12 imaging fields of view). During imaging sessions, mice were head-fixed under a two-photon microscope, and voluntarily ran on a spherical treadmill (Figure 1A). In a typical field of view, 39 ± 4 PV, 14 ± 7 SOM, and 323 ± 145 UNL neurons could be identified (mean ± s.d, Figures 2A and 2D).

The activity of inhibitory interneurons is strongly correlated with the activity of other inhibitory interneurons of the same subtype, across cortex.[17,22,25–27] To determine whether these patterns of activity relationships between pairs of individual SOM, PV, and UNL neurons hold in
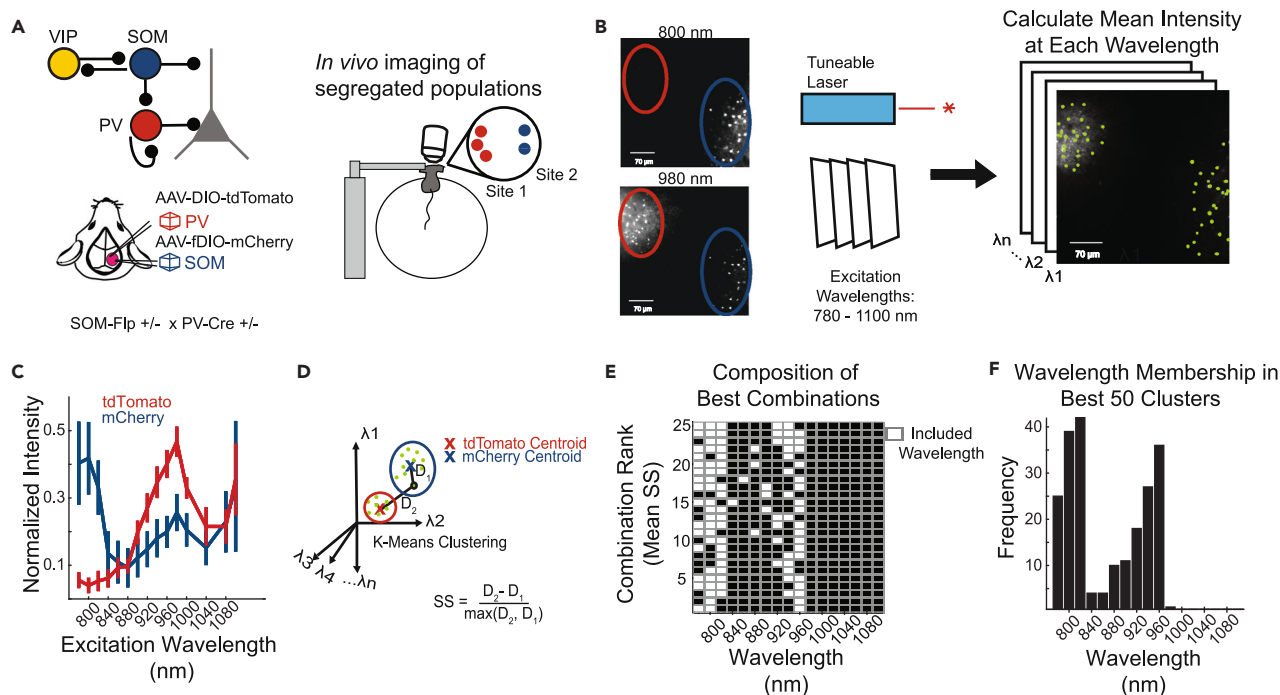
Figure 1. Validation of method to spectrally separate mCherry and tdTomato expressed in PV and SOM neurons *in vivo*

(A) SOM-Flp x PV-Cre mice received two adjacent, but physically segregated, injections of a Cre-dependent tdTomato and a Flp-dependent mCherry construct. For *in vivo* two-photon imaging, mice were head fixed on a spherical treadmill.

(B) A field of view was selected to include both the tdTomato (red circle) and mCherry (blue circle) injection sites. A series of images was collected, with excitation wavelengths ranging from 780 to 1100 nm. The mCherry site, but not the tdTomato site, was visible with 800 nm light (left), while both sites were visible with 980 nm excitation. ROIs were drawn over the cell bodies of the neurons to select pixels for analysis, indicated by green masks. Scale bars, 70 μm.

(C) Mean normalized intensity of tdTomato ROIs (red) and mCherry ROIs (blue), at all excitation wavelengths. Error bars indicate one standard deviation from the mean. The 1020 and 1060 nm wavelengths do not have values as they were not used (see STAR methods).

(D) Schematic of the clustering strategy to identify tdTomato+ and mCherry+ neurons, based on their excitation spectra. K-means clustering was performed on the vectors of mean intensity values for all ROIs, specifying that they should be clustered into two categories.

(E) K-means clustering was applied to the fluorescence of all mCherry and tdTomato ROIs collected at all possible combinations of two or more excitation wavelengths. For each combination, cluster separability was assessed by computing the mean of all silhouette scores, which is a measure of each ROI's distance to the centroids of the two clusters. The 25 best combinations of wavelengths (white rectangles) for cluster separability are shown here, ranked by their mean silhouette score.

(F) Frequency of a given wavelength occurring in the top 50 ranked combinations of wavelengths.

2 mice were used for panels C–F, with 6 different imaging sites across these animals, *n* = 326 ROIs.

mouse PPC, we computed Pearson correlations between each neuron pair across the imaging session, after discounting the effects of running velocity on each neuron's activity (see STAR methods). The distribution of pairwise correlations among cell type pairs was consistent with those previously observed in sensory cortex,[22,25,27] and SOM-SOM pairs were the most strongly and positively correlated (Figures 2E and 2F). Of all the cell type combinations, the least correlated pairs were the UNL-UNL pairs (Table S1).

Identifying periods of differential interneuron activity

Interneuron subtypes tended to be positively correlated with other neurons of the same type (Figures 2E and 2F). Strikingly, when visually inspecting the activity patterns in the simultaneously imaged PV and SOM neurons, we also observed spontaneous events of elevated firing across neurons that were restricted to one cell type or the other (Figures 2B and 3A). We hypothesized that PV and SOM activity events relate to different activity states in the local population.

First, to identify PV and SOM activity events, we used a peak finding algorithm to identify periods of elevated PV or SOM population activity and measured the mean activity of the other cell type population during this period (Figures 3A and S3A; see STAR methods). Because elevated activity periods of one IN subtype could occur either independently or concurrently with activity in the other subtype, we defined three types of events, based on the relative activity of SOM and PV. For SOM and PV events, the normalized activity of one cell type was more than double the opposing type. For "Mixed" events, the ratio between the types of activity was less than two (Figure 3B). SOM events, PV
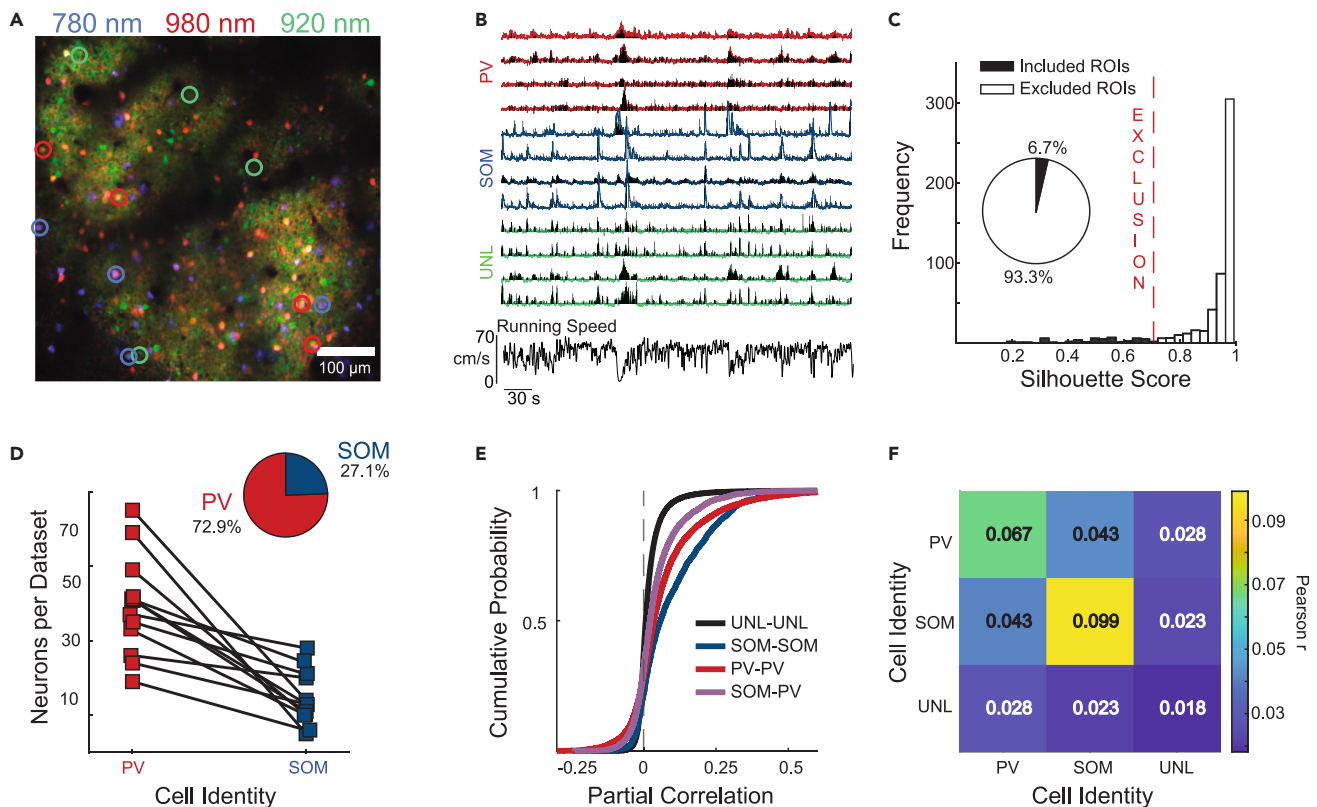
Figure 2. The strongest pairwise correlations are within interneuron subtypes

(A) Example field of view from layer 2/3 of PPC. The image is a merge of red fluorescence collected using 780 nm excitation (blue, visualizes mCherry+/SOM+ neurons), 980 nm (red, visualizes both mCherry+/SOM+ and tdTomato+/PV + neurons), and green fluorescence collected using 920 nm excitation (green, visualizes all neurons). Neurons with green but not red fluorescence were considered 'unlabeled' (UNL). Colored circles indicated cells used for the traces in (B). Scale bar, 100 μm.

(B) GCaMP fluorescence changes in a subset of the PV, SOM, and UNL neurons in the field of view in A (colored traces: red/PV, blue/SOM, and green/UNL). Black: estimated spike rates. Bottom: Time-aligned running speed of the mouse.

(C) Distribution of tdTomato/mCherry cluster separability (silhouette scores) for all red neurons. 0.7 was selected as an exclusion threshold, based on our estimate of our simulated noisy data (see Figure S2).

(D) Number of neurons classified as PV+/tdTomato+ and SOM+/mCherry+ in all datasets.

(E) Cumulative distribution function of all pairwise correlations taken between neurons across the entire imaging session. Pairwise correlations were computed as partial correlations, regressing off any shared activity due to running.

(F) Matrix showing the mean partial correlation within and between cell types. The mean correlation was significantly different between all non-symmetrical entries of the matrix. (See Table S1 for more detailed statistics).

Data are from 12 imaging sessions in 7 mice. Our labeling method yielded an average of 39 ± 4 PV, 14 ± 7 SOM, and 323 ± 145 UNL neurons per dataset (mean ± s.d.). Correlation results included 573661 pairs of UNL-UNL neurons, 1471 pairs of SOM-SOM, 10021 pairs of PV-PV, 6720 pairs of SOM-PV, 53661 pairs of UNL-SOM, and 135258 pairs of UNL-PV.

events, and "Mixed" events were not statistically different in their frequency or duration across categories (Figure 3C; see Table S2 for statistics).

PPC is involved in navigational decisions, and neural activity in PPC can be sensitive to the animal's running speed and direction.[17,28] While the mice in this study were not performing a task, they were running voluntarily on a spherical treadmill during imaging sessions. To determine whether PV, SOM, and Mixed activity events corresponded to behavioral events, we examined the running patterns of the mice. On average across mice, IN events corresponded to a small change in running acceleration; however, the mean peak of acceleration was not significantly different between event types and was not evident in all imaging sessions ($p = 1.0$, Kruskal-Wallis; Figure S4).

Next, to relate IN activity events to overall population activity levels, we examined the activity of the unlabeled, remaining neural population (UNL) during SOM, PV, and Mixed events. Activity in UNL neurons (which excludes neurons labeled as PV or SOM) was elevated during all three types of IN events; however, mean UNL activity was significantly higher during PV and Mixed events compared to SOM events (dF/F mean ± s.d.: 0.21 ± 0.09 SOM, 0.23 ± 0.09 PV, 0.24 ± 0.09 Mixed; SOM/Mixed and SOM/PV $p = 0.001$, Wilcoxon Sign-Rank) but was not statistically different between PV and Mixed events ($p = 0.52$; Figures 3E and 3F). We plotted the time course of mean activity scaled to its peak for each event, revealing that the peak activity of SOM neurons, which is likely the result of pooled input from local pyramidal neurons,[4] lagged
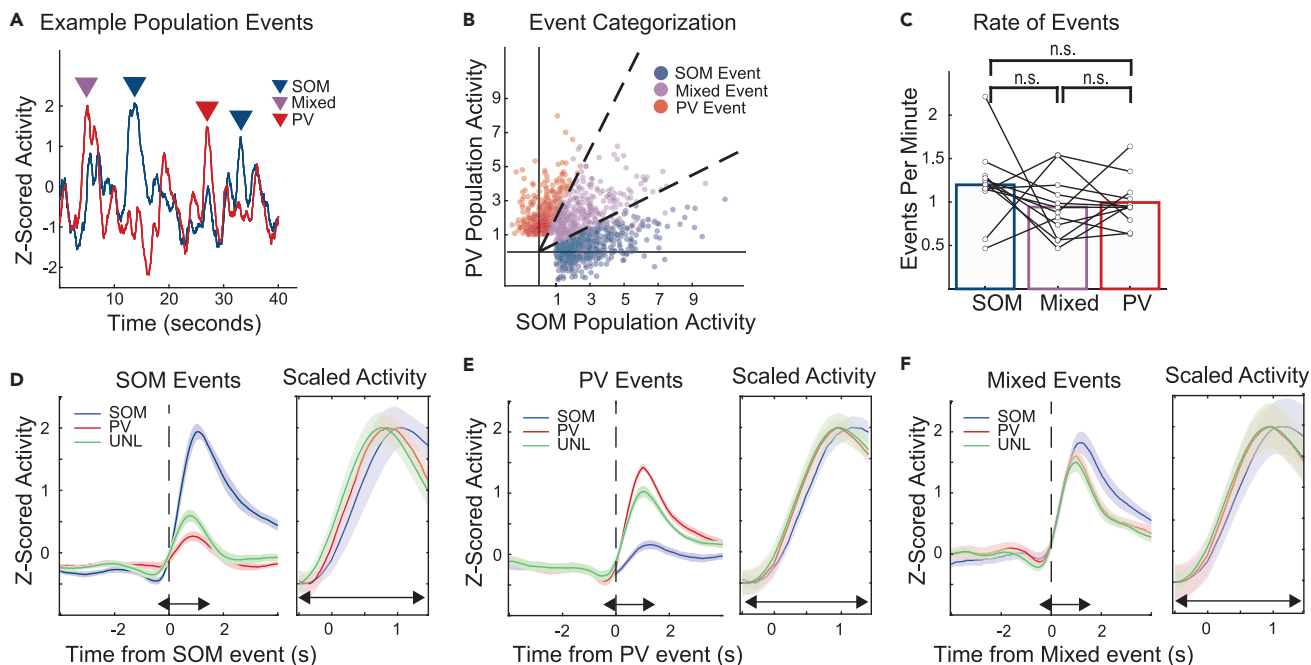
Figure 3. Interneuron event identification and timescale of mean activity during events

(A) Normalized population activity in simultaneously imaged SOM (blue) and PV (red) neurons (z-scored and averaged across neurons). Coordinated activity events were defined as peaks of activity that were unique to one population. Arrows above the activity traces mark these peaks.

(B) SOM population activity plotted against PV population activity during events across all datasets (red: PV events, blue: SOM events, purple: Mixed).

(C) Rate of events per minute. Bars indicate mean across datasets, circles indicate individual datasets. There was no significant difference between event types.

(D) Activity of the SOM, PV, and UNL neurons aligned to the onset of SOM events. The mean activity for each cell type is z-scored across the entire session for each dataset, and then averaged across all events for each cell type. Shading indicates s.e.m.

(E and F) As in D, but for PV and Mixed events.

For all panels, "n.s." means non-significant. Data comes from 12 imaging sessions in 7 animals, which yielded 430 SOM events, 400 PV events, and 387 Mixed events across all sessions.

mean PV activity by ∼200 ms during SOM (mean lag: 0.24 s, $p = 0.042$, Wilcoxon signed-rank) and Mixed events (Mean lag 0.17 s, $p = 0.012$), reflecting previously observed dynamics in V1.[2,29] In contrast, SOM activity did not lag behind PV activity during PV events (mean lag: 0.03 s, $p = 0.50$), potentially reflecting its reduced activity relative to PV.

Comparing network states during differential periods of IN activity

When PV and SOM neurons are optogenetically stimulated as populations, they have different effects on local population activity dynamics[11,14] and in shaping the response properties of individual neurons.[2,8,9,30] So far, our results suggest that PV and SOM neurons can act naturally as highly coordinated and independent subpopulations. In the current study, we also have the unique opportunity to determine the changes in the local network activity state that accompany these natural bursts in PV, SOM, or PV and SOM population activity.

We examined the activity of individual UNL neurons during IN events, by binning their activity from the peak of the event until 2 s after the IN activity peak. This accounted for most of the period of elevated IN activity across events (Figure S3D; Table S2). Consistent with the preferential connectivity and activity relationships between some pyramidal neurons and specific inhibitory cell types,[20,25,31] we did find small subsets of individual UNL neurons that tended to be more active either during SOM or PV events, as measured by increases in their mean activity during PV or SOM events (Figure 4A). Although the majority of individual UNL neurons (80%) had no response preference, 17% of UNL neurons had significantly higher firing during PV events and 4% of neurons significantly higher firing during SOM events (Figure S5A; significance determined by $p < 0.05$ from a permutation test between firing rates for SOM and PV events). Activity of SOM-preferring neurons was significantly less correlated with the population than activity of PV-preferring neurons ($p < 6.14*10^{-8}$, Wilcoxon rank-sum) or of neurons without preference ($p = 0.016$) over periods of non-event activity (Figure S5A). SOM-preferring and PV-preferring neurons were more correlated with other neurons with similar preferences than with neurons that had opposing preferences ($p = 4.8 \times 10^{4}$ for PV-PV vs. SOM-PV and for SOM-SOM vs. SOM-PV, Wilcoxon signed-rank), suggesting that these UNL subsets may form functional subnetworks that are relevant outside of IN events (Figure S5B).

Previous work that has shown that functionally relevant subnetworks of INs can be identified based on how they are driven by pyramidal activity.[31] Given the preference of UNL neurons' activity for a particular IN event type, we hypothesized that PV and SOM events could be
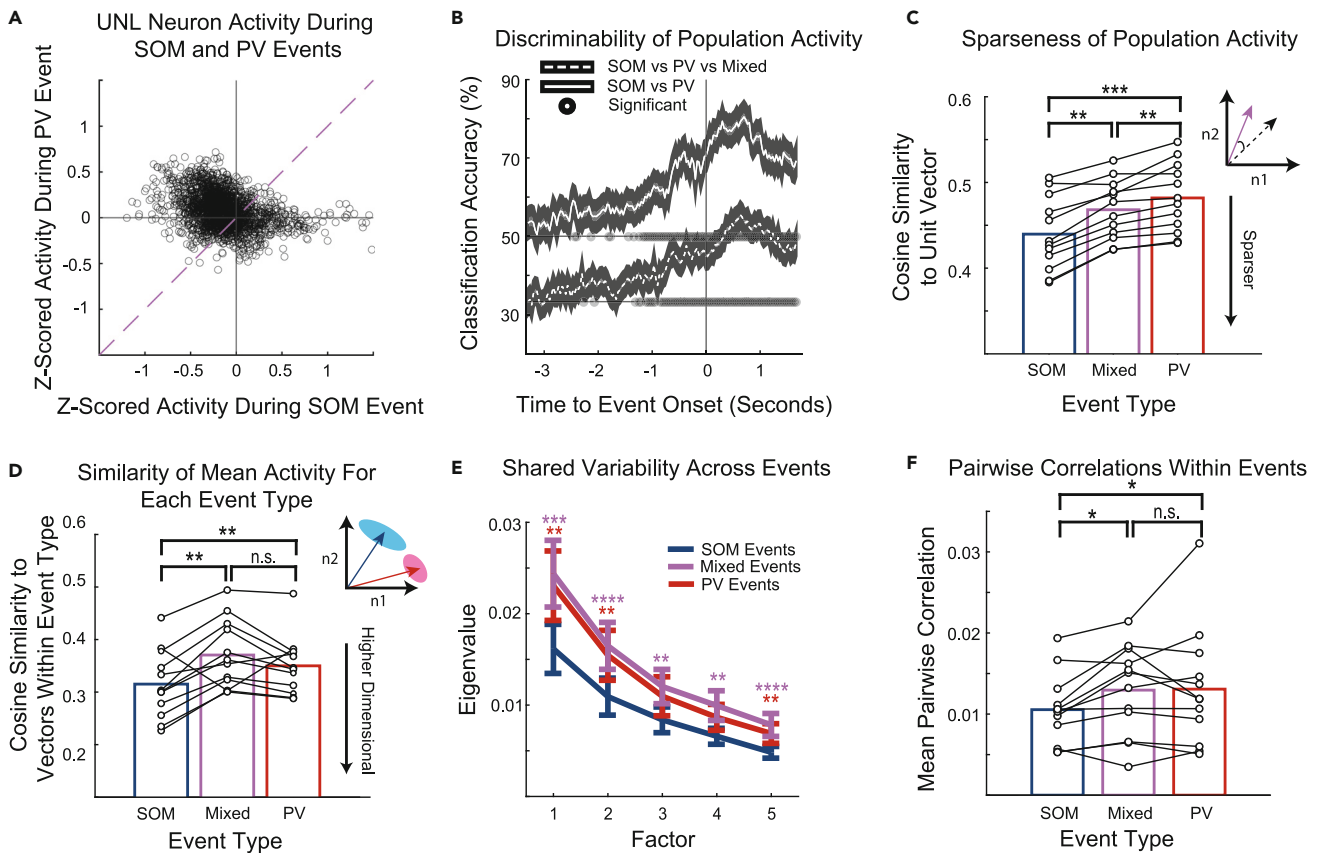
Figure 4. PV, SOM, and Mixed events are associated with different local population activity states

(A) Mean normalized activity for each UNL neuron during PV and SOM events. The activity of UNL neurons for each event was z-scored across all PV and SOM events for each neuron, and the mean of this z-scored activity was plotted. The unity line would indicate equal activity of neurons during SOM and PV events.

(B) Performance of decoders trained to distinguish between SOM and PV events, or SOM, PV and Mixed events based on the mean activity during 333 ms bins (each plotted time point is based on bins that start at that time point and end 333 ms later). Shaded circles indicate classification accuracy that was significantly ($p < 0.05$) greater than the performance of a classifier with randomly shuffled labels for training, after Bonferonni correction for multiple comparisons at all 150 time points.

(C) Sparseness of unlabeled neuron population activity, measured by the mean angle between all vectors for an event type and the unit vector, which corresponds to all neurons being equivalently active. Vectors included each neuron's activity, binned over 2 s following the event peak.

(D) Pairwise cosine similarity of mean activity vectors 2s after the peak of the event. Pairwise similarity of unlabeled population activity during SOM events was significantly lower than during PV events, indicating population activity spanned a wider space of possible activity patterns during SOM events.

(E) Factor analysis was able to explain more shared variability in unlabeled neuron population activity during PV and Mixed events compared to SOM events. Purple stars indicate significance between SOM and Mixed events, while red stars indicate significance between SOM and PV events. Factor analysis was performed 5 times on each dataset, subsampling 75 UNL neurons each time. Error bars indicate standard error of the mean.

(F) Pairwise correlations calculated between unlabeled neurons during the 2 s after the peak for each event. The mean pairwise correlation was significantly higher during PV and Mixed events compared to SOM events across datasets.

For all panels, n.s. means no significance; *, $p < 0.05$; **, $p < 0.01$; ***, $p < 0.001$, ****, $p < 0.0001$. Data comes from 12 imaging sessions in 7 animals, which yielded 430 SOM events, 400 PV events, and 387 Mixed events across all sessions.

predicted by the pattern of UNL activity, even before the IN event onset. We aligned neural activity to IN event onsets and trained support vector machines (SVMs) to classify events as SOM, PV, or Mixed using the vector of UNL population activity at each time point during the event. Classification performance rose above chance levels more than 1 s before the IN event onset (Figure 4B; see STAR methods), and then peaked 0.70 and 0.63 s after the onset for the two- and three-way classifiers, respectively (Figure 4B). Control analyses revealed classification was not explained by differences in mean activity, as the mean vector across all trials was approximately parallel to the decision boundary in each dataset for each classification method (Figures S5C and S5D). Together, the classification results suggest that specific patterns of activity in the local population precede PV and SOM events. Although the origin of that difference is unclear from our study, it could reflect changes in the activity of extrinsic sources of input or neuromodulatory tone.

Populations of neurons can encode information with varying levels of sparseness. This continuum ranges from dense codes, where all neurons more equally contribute, to local codes where only a small proportion of neurons are active.[32] We hypothesized, based on

previous results where optogenetic activation of SOM cells increases sparsity of sensory responses,[14] that UNL population activity would be sparser during SOM events than during PV events. To examine the sparsity of population activity, we examined the angle between the mean UNL population vector during events to the unit vector, which would correspond to all UNL neurons in the population being equally active. A greater angle between two population vectors suggests that the relative activity between neurons in the population is less similar.[14,32,33] Therefore, in comparing a UNL population activity vector measured during IN events to the unit vector, we can determine the similarity between the actual pattern of activity and a dense code (the unit vector). We report these angles in terms of cosine similarity, where an angle of zero between the vectors would indicate identical ratios of activity between neurons, and result in a cosine similarity of one. The cosine similarity between the unit vector and the UNL population activity vector during SOM events was lower than during Mixed or PV events ($p = 0.0015$, $p = 0.00049$, Wilcoxon signed-rank), suggesting that UNL activity was sparser during SOM events (Figure 4C). In tandem with increased sparseness, in auditory cortex SOM neuron stimulation increases the angle between mean population vectors in response to different stimuli, enhancing the separability of evoked population activity patterns.[14] We observed a similar effect during spontaneous activity in PPC, as the pairwise similarity between population activity vectors was lowest across SOM events than other IN event types (SOM/PV, $p = 0.0049$; SOM/Mixed, $p = 0.0044$; PV/Mixed, $p = 0.09$, Wilcoxon signed-rank; Figure 4D). This indicates that more population states were possible during events with both higher SOM neuron activity and lower PV neuron activity.

Our results indicate that UNL neurons fired more independently when SOM activity was high and PV was low, reflected by increased sparseness and variability of UNL neuron activity across SOM activity events. Prior work in V1 has shown that SOM neuron stimulation can modulate the coherence of population activity, lowering pairwise activity correlations between neurons.[11] Pairwise correlations between UNL neurons were indeed lower during SOM events compared to PV or Mixed events (SOM/PV, $p = 0.020$, SOM/Mixed, $p = 0.032$; PV/Mixed, $p = 0.070$, Wilcoxon signed-rank; Figure S5E), which is consistent with the decorrelating effect of optogenetic stimulation of SOM neurons on the rest of the population.[11] Shared variability tends to be low-dimensional, where a large proportion of shared variability can be explained by a single latent variable.[34] To compare the dimensionality of shared variability within the UNL population during SOM, PV, and Mixed events, we used factor analysis to find axes in high dimensional space along which many neurons covary. The top five latent factors explained less shared variability across all periods of time during SOM events, indicating pyramidal neurons acted more independently during these times (Figure 4E; see Table S3 for statistics). Since these results could be explained either by our finding that the mean activity during SOM events can occupy more possible states, or a reduction in covariance between neurons on shorter timescales during an event, we additionally took pairwise correlations of the mean-subtracted activity between neurons within each individual event, for only active neurons. UNL neurons had lower correlations within SOM events than Mixed or PV events (SOM/PV, $p = 0.015$, SOM/Mixed, $p = 0.032$; PV/Mixed, $p = 0.77$, Wilcoxon signed-rank; Figure 4F), suggesting our results from factor analysis were explained by lower moment-to-moment fluctuations shared between neurons as well as the comparatively greater span of neural activity across SOM events.

DISCUSSION

Here, we have demonstrated a simple and reliable method for distinguishing two red fluorophores *in vivo*, leveraging differences in their excitation spectra. The method allowed us to monitor the activity of two specific inhibitory cells along with the rest of the neural population, using a standard two-photon microscope with two detection channels. This enables analysis methods to parse how interactions between interneurons, which can strongly connect to one another,[13] affect activity in the broader neural population. When combined with experiments using optogenetic stimulation, the presentation of sensory stimuli, or involving goal-directed behavior, this will allow a more complete explanation of neural activity and its connection to behavior on individual trials.

Past research in sensory cortex has shown that IN activity tends to be highly coordinated, especially within cell type.[17,25,27] Our results in PPC, an association area that integrates multimodal sensory input,[35–37] demonstrate this may be a general feature in cortical circuits. By labeling the two IN subtypes that strongly inhibit different compartments of pyramidal cells,[4] we could isolate periods of time when coordinated IN activity occurred and characterize the cooccurring network activity state in the unlabeled neural population, which largely consisted of pyramidal cells, during PV and SOM events. This would not have been possible by labeling one IN at a time: UNL neuron population activity during Mixed events resembled PV events more closely than SOM events (Figures 4C–4F and S5E), even though SOM activity was also relatively high in Mixed events (Figure 3B). Our labeling also revealed UNL neurons that responded preferentially during either PV or SOM events (Figure 4A). PV- and SOM-event preferring neurons were differently correlated with the rest of the local population: neurons with the same response preference were strongly correlated with one another, but not with neurons of opposite preference, suggesting PV- and SOM-preferring neurons may form functional subnetworks (Figures S5A and S5B).[25] Surprisingly, the pattern of UNL neuron population activity could predict the identity of PV vs. SOM activity events up to 1 s before the events (Figure 4B). We cannot determine in this study whether the SOM and PV events were triggered by local UNL neuron activity or whether both were commonly driven by extrinsic inputs, but future experiments using optogenetic stimulation of specific ensembles of neurons could test whether local activity can drive specific IN events.

The information that can be encoded by populations of neurons is constrained by the correlation structure of their activity, by restricting the number of possible states a population can occupy.[38] This reduction in states due to the dependence between neurons can be conceptualized as lowering the dimensionality of population activity.[39] Across analyses at different time scales of the event types, a general pattern emerged in our study, where activity among unlabeled neurons was more independent when SOM activity was high than when

PV activity was high. This was reflected in more sparse activity during SOM events (Figure 4C) that could span a broader set of population states (Figure 4D). Factor analysis was better able to summarize the population with fewer dimensions across all PV events, and within events pairwise correlations were lower from moment-to-moment (Figures 4E and 4F). This is despite the fact that SOM neurons are more coordinated in their activity (Figure 2E; Table S1), which would indicate a priori that activity states identified by their mean activity would be more homogeneous.

Our findings of increased independence of activity across UNL neurons with greater SOM neuron activity are corroborated by similar results from auditory and visual cortex in response to optogenetic stimulation,[11,14] as well as increased SOM activity from larger stimuli.[40] These studies have also noted the suppression of PV neurons corresponding to the population effects observed from elevated SOM activity,[2,9,40] and one model found the inhibition of PV by SOM to be essential for explaining the effect.[2] In our data from association cortex, we observed more independent activity only when mean SOM activity was relatively high and mean PV activity was relatively low. While far from conclusive, this suggests that there is a conserved microcircuit involving SOM and PV neurons that can influence the independence of neural activity in different cortical areas. One potential mechanism comes from the distinct modes of inhibition provided by SOM and PV neurons, where inhibition of distal dendrites from SOM neurons may reduce recurrent excitation received from surrounding pyramidal neurons, allowing them to act more independent of one another.[40]

Controlling the correlations between neurons or dimensionality of the population has broad implications for the neural code. Depending on their structure, correlations can negatively influence the resolution of stimulus encoding,[38,41–43] and can be modified by attention and learning to improve task performance.[44,45] However, the relationship between correlations and behavioral performance is inverted in PPC,[46,47] seeming to sacrifice the resolution of information for better signal propagation.[43] Given the similarities between IN activity and correlations from our data in PPC compared to sensory cortex, modulatory input to interneurons in PPC may be different relative to sensory areas to best drive population activity and behavior. Further efforts to understand the underlying circuitry will better allow us to make predictions about how the brain achieves population dynamics that serve the processing demands of an individual brain region.

Limitations of the study

Our analysis in this paper is strictly correlational. We did not control input to the network with sensory stimuli, goal-directed behavior, or optogenetics. Consequently, from our results alone we cannot conclude whether the relationships between local population activity and SOM and PV events are causal, or driven by common factors. Future studies combining our approach with behavioral tasks, causal manipulations, such as optogenetic stimulation of PV or SOM neurons, or of specific ensembles of pyramidal neurons, can be used to test these relationships.

The naturally occurring inhibitory population events that we detected in our study occurred spontaneously, and SOM-dominated vs. PV-dominated events were associated with highly different local network dynamics. This is in agreement with results from other studies, where optogenetic stimulation of the full population of either PV or SOM neurons had differing impacts on local network coherence.[11,14] Our results suggest that these network-level effects of PV and SOM activity occur naturally, and are not simply the result of the highly artificial and synchronous nature of full-field optogenetic stimulation. Because the events in our study occurred spontaneously, relatively infrequently (a few events per minute), and were not strongly associated with any observable behavioral changes, we cannot draw conclusions about their behavioral relevance, if any. Future studies relating the frequency of PV and SOM events to arousal state or task performance will be important to help uncover the behavioral relevance of these activity states.

We additionally used only the mean activity of interneurons to make conclusions about the functions of cell types. As shown by recent experiments, there is heterogeneity within cell types that will not be captured by the mean.[48] A more complete understanding of the function of these neuron classes will need to come from combining our approach with more controlled experiments such as perceptual decision-making tasks, which allow for looking at INs based on their function as they correspond to task performance or stimulus features. A further application of our labeling strategy could be to label the full SOM population, and a genetic subclass of SOM neurons with mCherry and tdTomato.

In our study, we relied on the cell-type expression of Cre and Flp to identify PV and SOM neurons. Some non-specific expression of Cre- and Flp-dependent reporters has been observed in excitatory cells in these mice, especially when the Cre-dependent reporters have been expressed transgenically.[18,49] Even in our viral approach, a small minority of tdTomato or mCherry neurons could be excitatory neurons that have been mislabeled. However, our approach relies on identifying population-wide activity events across these IN populations, and so small numbers of misidentified excitatory neurons are unlikely to affect our results.

Finally, we cannot be certain of the cell type identity of the "unlabeled" neurons in our populations. While pyramidal neurons are by far the most numerous cell type that does not express PV or SOM, we cannot rule out the possibility that VIP neurons contribute to the functional subclasses of UNL neurons that become active preferentially during PV or SOM events.

RESOURCE AVAILABILITY

Lead contact

Further information and requests for resources and reagents should be directed to and will be fulfilled by the lead contact, Caroline A. Runyan (runyan@pitt.edu).

Materials availability

This study did not generate unique new reagents.

Data and code availability

- Data have been deposited at Mendeley Data and are publicly available as of the date of publication. Accession numbers are listed in the key resources table.
- All original code has been deposited at Github and is publicly available as of the date of publication. DOIs are listed in the key resources table.
- Any additional information required to reanalyze the data reported in this paper is available from the lead contact upon request.

AUTHOR CONTRIBUTIONS

C.A.R. and C.T.P. designed the experiments. C.D.B. conducted experiments. C.D.B. and C.T.P. processed data. C.T.P. performed analyses. C.A.R., C.D.B., and C.T.P. wrote the paper.

DECLARATION OF INTERESTS

The authors declare no competing interests.

STAR★METHODS

Detailed methods are provided in the online version of this paper and include the following:

- KEY RESOURCES TABLE
- EXPERIMENTAL MODEL AND STUDY PARTICIPANT DETAILS
- METHOD DETAILS
  - Surgery
  - Control surgery
  - Two-photon microscope
  - Behavioral monitoring
  - Image acquisition
  - Image Processing
  - mCherry and tdTomato ROI classification
  - GCaMP fluorescence processing
  - dF/F and deconvolution
  - Pairwise correlations
  - Identification of PV and SOM population events
  - Event type classification
  - Population vector cosine similarity
  - Factor analysis
  - Histology
- QUANTIFICATION AND STATISTICAL ANALYSIS

SUPPLEMENTAL INFORMATION

Supplemental information can be found online at https://doi.org/10.1016/j.isci.2024.110736.

REFERENCES

1. Isaacson, J.S., and Scanziani, M. (2011). How Inhibition Shapes Cortical Activity. Neuron 72, 231–243. https://doi.org/10.1016/j.neuron.2011.09.027.

2. Rikhye, R.V., Yildirim, M., Hu, M., Breton-Provencher, V., and Sur, M. (2021). Reliable Sensory Processing in Mouse Visual Cortex through Cooperative Interactions between Somatostatin and Parvalbumin Interneurons. J. Neurosci. 41, 8761–8778. https://doi.org/10.1523/jneurosci.3176-20.2021.

3. Kepecs, A., and Fishell, G. (2014). Interneuron cell types are fit to function. Nature 505, 318–326. https://doi.org/10.1038/nature12983.

4. Tremblay, R., Lee, S., and Rudy, B. (2016). GABAergic Interneurons in the Neocortex: From Cellular Properties to Circuits. Neuron 91, 260–292. https://doi.org/10.1016/j.neuron.2016.06.033.

5. Yoshimura, Y., and Callaway, E.M. (2005). Fine-scale specificity of cortical networks depends on inhibitory cell type and connectivity. Nat. Neurosci. 8, 1552–1559. https://doi.org/10.1038/nn1565.

6. Znamenskiy, P., Kim, M.-H., Muir, D.R., Iacaruso, M.F., Hofer, S.B., and Mrsic-Flogel, T.D. (2024). Functional specificity of recurrent inhibition in visual cortex. Neuron 112, 991–1000.e8. https://doi.org/10.1016/j.neuron.2023.12.013.

7. Atallah, B.V., Bruns, W., Carandini, M., and Scanziani, M. (2012). Parvalbumin-Expressing Interneurons Linearly Transform Cortical Responses to Visual Stimuli. Neuron 73, 159–170. https://doi.org/10.1016/j.neuron.2011.12.013.

8. Wilson, N.R., Runyan, C.A., Wang, F.L., and Sur, M. (2012). Division and subtraction by distinct cortical inhibitory networks in vivo. Nature 488, 343–348. https://doi.org/10.1038/nature11347.

9. Adesnik, H., Bruns, W., Taniguchi, H., Huang, Z.J., and Scanziani, M. (2012). A neural circuit for spatial summation in visual cortex. Nature *490*, 226–231. https://doi.org/10.1038/nature11526.

10. Zhang, S., Xu, M., Kamigaki, T., Hoang Do, J.P., Chang, W.-C., Jenvay, S., Miyamichi, K., Luo, L., and Dan, Y. (2014). Long-range and local circuits for top-down modulation of visual cortex processing. Science *345*, 660–665. https://doi.org/10.1126/science.1254126.

11. Chen, N., Sugihara, H., and Sur, M. (2015). An acetylcholine-activated microcircuit drives temporal dynamics of cortical activity. Nat. Neurosci. *18*, 892–902. https://doi.org/10.1038/nn.4002.

12. Wang, X.-J., and Yang, G.R. (2018). A disinhibitory circuit motif and flexible information routing in the brain. Curr. Opin. Neurobiol. *49*, 75–83. https://doi.org/10.1016/j.conb.2018.01.002.

13. Pfeffer, C.K., Xue, M., He, M., Huang, Z.J., and Scanziani, M. (2013). Inhibition of inhibition in visual cortex: the logic of connections between molecularly distinct interneurons. Nat. Neurosci. *16*, 1068–1076. https://doi.org/10.1038/nn.3446.

14. Tobin, M., Sheth, J., Wood, K.C., and Geffen, M.N. (2023). Localist versus Distributed Representation of Sounds in the Auditory Cortex Controlled by Distinct Inhibitory Neuronal Subtypes. Preprint at bioRxiv. https://doi.org/10.1101/2023.02.01.526470.

15. Kuchibhotla, K.V., Gill, J.V., Lindsay, G.W., Papadoyannis, E.S., Field, R.E., Sten, T.A.H., Miller, K.D., and Froemke, R.C. (2017). Parallel processing by cortical inhibition enables context-dependent behavior. Nat. Neurosci. *20*, 62–71. https://doi.org/10.1038/nn.4436.

16. Dipoppa, M., Ranson, A., Krumin, M., Pachitariu, M., Carandini, M., and Harris, K.D. (2018). Vision and Locomotion Shape the Interactions between Neuron Types in Mouse Visual Cortex. Neuron *98*, 602–615.e8. https://doi.org/10.1016/j.neuron.2018.03.037.

17. Khoury, C.F., Fala, N.G., and Runyan, C.A. (2022). The spatial scale of somatostatin subnetworks increases from sensory to association cortex. Cell Rep. *40*, 111319. https://doi.org/10.1016/j.celrep.2022.111319.

18. Hofer, S.B., Ko, H., Pichler, B., Vogelstein, J., Ros, H., Zeng, H., Lein, E., Lesica, N.A., and Mrsic-Flogel, T.D. (2011). Differential connectivity and response dynamics of excitatory and inhibitory neurons in visual cortex. Nat. Neurosci. *14*, 1045–1052. https://doi.org/10.1038/nn.2876.

19. Kerlin, A.M., Andermann, M.L., Berezovskii, V.K., and Reid, R.C. (2010). Broadly Tuned Response Properties of Diverse Inhibitory Neuron Subtypes in Mouse Visual Cortex. Neuron *67*, 858–871. https://doi.org/10.1016/j.neuron.2010.08.002.

20. Condylis, C., Ghanbari, A., Manjrekar, N., Bistrong, K., Yao, S., Yao, Z., Nguyen, T.N., Zeng, H., Tasic, B., and Chen, J.L. (2022). Dense functional and molecular readout of a circuit hub in sensory cortex. Science *375*, eabl5981. https://doi.org/10.1126/science.abl5981.

21. Poort, J., Wilmes, K.A., Blot, A., Chadwick, A., Sahani, M., Clopath, C., Mrsic-Flogel, T.D., Hofer, S.B., and Khan, A.G. (2022). Learning and attention increase visual response selectivity through distinct mechanisms.

Neuron *110*, 686–697.e6. https://doi.org/10.1016/j.neuron.2021.11.016.

22. Bugeon, S., Duffield, J., Dipoppa, M., Ritoux, A., Prankerd, I., Nicoloutsopoulos, D., Orme, D., Shinn, M., Peng, H., Forrest, H., et al. (2022). A transcriptomic axis predicts state modulation of cortical interneurons. Nature *607*, 330–338. https://doi.org/10.1038/s41586-022-04915-7.

23. Drobizhev, M., Tillo, S., Makarov, N.S., Hughes, T.E., and Rebane, A. (2009). Absolute Two-Photon Absorption Spectra and Two-Photon Brightness of Orange and Red Fluorescent Proteins. J. Phys. Chem. B *113*, 855–859. https://doi.org/10.1021/jp8087379.

24. Chen, T.-W., Wardill, T.J., Sun, Y., Pulver, S.R., Renninger, S.L., Baohan, A., Schreiter, E.R., Kerr, R.A., Orger, M.B., Jayaraman, V., et al. (2013). Ultrasensitive fluorescent proteins for imaging neuronal activity. Nature *499*, 295–300. https://doi.org/10.1038/nature12354.

25. Karnani, M.M., Jackson, J., Ayzenshtat, I., Tucciarone, J., Manoocheri, K., Snider, W.G., and Yuste, R. (2016). Cooperative Subnetworks of Molecularly Similar Interneurons in Mouse Neocortex. Neuron *90*, 86–100. https://doi.org/10.1016/j.neuron.2016.02.037.

26. Khan, A.G., Poort, J., Chadwick, A., Blot, A., Sahani, M., Mrsic-Flogel, T.D., and Hofer, S.B. (2018). Distinct learning-induced changes in stimulus selectivity and interactions of GABAergic interneuron classes in visual cortex. Nat. Neurosci. *21*, 851–859. https://doi.org/10.1038/s41593-018-0143-z.

27. Knoblich, U., Huang, L., Zeng, H., and Li, L. (2019). Neuronal cell-subtype specificity of neural synchronization in mouse primary visual cortex. Nat. Commun. *10*, 2533. https://doi.org/10.1038/s41467-019-10498-1.

28. Minderer, M., Brown, K.D., and Harvey, C.D. (2019). The Spatial Structure of Neural Encoding in Mouse Posterior Cortex during Navigation. Neuron *102*, 232–248.e11. https://doi.org/10.1016/j.neuron.2019.01.029.

29. El-Boustani, S., and Sur, M. (2014). Response-dependent dynamics of cell-specific inhibition in cortical networks in vivo. Nat. Commun. *5*, 5689. https://doi.org/10.1038/ncomms6689.

30. Phillips, E.A.K., Schreiner, C.E., and Hasenstaub, A.R. (2017). Cortical Interneurons Differentially Regulate the Effects of Acoustic Context. Cell Rep. *20*, 771–778. https://doi.org/10.1016/j.celrep.2017.07.001.

31. Palagina, G., Meyer, J.F., and Smirnakis, S.M. (2019). Inhibitory Units: An Organizing Nidus for Feature-Selective SubNetworks in Area V1. J. Neurosci. *39*, 4931–4944. https://doi.org/10.1523/jneurosci.2275-18.2019.

32. Vinje, W.E., and Gallant, J.L. (2000). Sparse Coding and Decorrelation in Primary Visual Cortex During Natural Vision. Science *287*, 1273–1276. https://doi.org/10.1126/science.287.5456.1273.

33. Buschman, T.J., and Kastner, S. (2015). From Behavior to Neural Dynamics: An Integrated Theory of Attention. Neuron *88*, 127–144. https://doi.org/10.1016/j.neuron.2015.09.017.

34. Ruff, D.A., Xue, C., Kramer, L.E., Baqai, F., and Cohen, M.R. (2020). Low rank mechanisms underlying flexible visual representations. Proc. Natl. Acad. Sci. USA *117*, 29321–29329. https://doi.org/10.1073/pnas.2005797117.

35. Zingg, B., Hintiryan, H., Gou, L., Song, M.Y., Bay, M., Bienkowski, M.S., Foster, N.N., Yamashita, S., Bowman, I., Toga, A.W., and Dong, H.W. (2014). Neural Networks of the Mouse Neocortex. Cell *156*, 1096–1111. https://doi.org/10.1016/j.cell.2014.02.023.

36. Lyamzin, D., and Benucci, A. (2019). The mouse posterior parietal cortex: Anatomy and functions. Neurosci. Res. *140*, 14–22. https://doi.org/10.1016/j.neures.2018.10.008.

37. Song, Y.-H., Kim, J.-H., Jeong, H.-W., Choi, I., Jeong, D., Kim, K., and Lee, S.-H. (2017). A Neural Circuit for Auditory Dominance over Visual Perception. Neuron *93*, 940–954.e6. https://doi.org/10.1016/j.neuron.2017.01.006.

38. Stringer, C., Pachitariu, M., Steinmetz, N., Carandini, M., and Harris, K.D. (2019). High-dimensional geometry of population responses in visual cortex. Nature *571*, 361–365. https://doi.org/10.1038/s41586-019-1346-5.

39. Cunningham, J.P., and Yu, B.M. (2014). Dimensionality reduction for large-scale neural recordings. Nat. Neurosci. *17*, 1500–1509. https://doi.org/10.1038/nn.3776.

40. Angelucci, A., Bijanzadeh, M., Nurminen, L., Federer, F., Merlin, S., and Bressloff, P.C. (2017). Circuits and Mechanisms for Surround Modulation in Visual Cortex. Annu. Rev. Neurosci. *40*, 425–451. https://doi.org/10.1146/annurev-neuro-072116-031418.

41. Goard, M., and Dan, Y. (2009). Basal forebrain activation enhances cortical coding of natural scenes. Nat. Neurosci. *12*, 1444–1449. https://doi.org/10.1038/nn.2402.

42. Ni, A.M., Huang, C., Doiron, B., and Cohen, M.R. (2022). A general decoding strategy explains the relationship between behavior and correlated variability. Elife *11*, e67258. https://doi.org/10.7554/elife.67258.

43. Panzeri, S., Moroni, M., Safaai, H., and Harvey, C.D. (2022). The structures and functions of correlations in neural population codes. Nat. Rev. Neurosci. *23*, 551–567. https://doi.org/10.1038/s41583-022-00606-4.

44. Ni, A.M., Ruff, D.A., Alberts, J.J., Symmonds, J., and Cohen, M.R. (2018). Learning and attention reveal a general relationship between population activity and behavior. Science *359*, 463–465. https://doi.org/10.1126/science.aao0284.

45. McBride, E.G., Lee, S.-Y.J., and Callaway, E.M. (2019). Local and Global Influences of Visual Spatial Selection and Locomotion in Mouse Primary Visual Cortex. Curr. Biol. *29*, 1592–1605.e5. https://doi.org/10.1016/j.cub.2019.03.065.

46. Runyan, C.A., Piasini, E., Panzeri, S., and Harvey, C.D. (2017). Distinct timescales of population coding across cortex. Nature *548*, 92–96. https://doi.org/10.1038/nature23020.

47. Valente, M., Pica, G., Bondanelli, G., Moroni, M., Runyan, C.A., Morcos, A.S., Harvey, C.D., and Panzeri, S. (2021). Correlations enhance the behavioral readout of neural population activity in association cortex. Nat. Neurosci. *24*, 975–986. https://doi.org/10.1038/s41593-021-00845-1.

48. Green, J., Bruno, C.A., Traunmüller, L., Ding, J., Hrvatin, S., Wilson, D.E., Khodadad, T., Samuels, J., Greenberg, M.E., and Harvey, C.D. (2023). A cell-type-specific error-correction signal in the posterior parietal cortex. Nature *620*,

366–373. https://doi.org/10.1038/s41586-023-06357-1.

49. Müller-Komorowska, D., Opitz, T., Elzoheiry, S., Schweizer, M., Ambrad Giovannetti, E., and Beck, H. (2020). Nonspecific Expression in Limited Excitatory Cell Populations in Interneuron-Targeting Cre-driver Lines Can Have Large Functional Effects. Front. Neural Circ. *14*, 16. https://doi.org/10.3389/fncir.2020.00016.

50. Pachitariu, M., Stringer, C., Dipoppa, M., Schröder, S., Rossi, L.F., Dalgleish, H., Carandini, M., and Harris, K.D. (2017). Suite2p: beyond 10,000 neurons with standard two-photon microscopy. Preprint at bioRxiv. https://doi.org/10.1101/061507.

51. Stringer, C., Wang, T., Michaelos, M., and Pachitariu, M. (2021). Cellpose: a generalist algorithm for cellular segmentation. Nat. Methods *18*, 100–106. https://doi.org/10.1038/s41592-020-01018-x.

52. Friedrich, J., Zhou, P., and Paninski, L. (2017). Fast online deconvolution of calcium imaging data. PLoS Comput. Biol. *13*, e1005423.

53. Yu, B.M., Cunningham, J.P., Santhanam, G., Ryu, S.I., Shenoy, K.V., and Sahani, M. (2009). Gaussian-Process Factor Analysis for Low-Dimensional Single-Trial Analysis of Neural Population Activity. J. Neurophysiol. *102*, 614–635. https://doi.org/10.1152/jn.90941.2008.

54. Huang, C., Ruff, D.A., Pyle, R., Rosenbaum, R., Cohen, M.R., and Doiron, B. (2019). Circuit Models of Low-Dimensional Shared Variability in Cortical Networks. Neuron *101*, 337–348.e4. https://doi.org/10.1016/j.neuron.2018.11.034.

STAR★METHODS

KEY RESOURCES TABLE

REAGENT or RESOURCE	SOURCE	IDENTIFIER
Bacterial and virus strains		
pAAV-Ef1a-fDIO-mCherry	Addgene	114471
pAAV-FLEX-tdTomato	Addgene	28306
pAAV.Syn.GCaMP6f.WPRE.SV40A	Addgene	100837
Deposited data		
dF/F, deconvolved, and behavioral data	This study	Mendeley Data: https://doi.org/10.17632/jx8p7cmkk3.1, https://doi.org/10.17632/54cf564b9h.1
Experimental models: Organisms/strains		
B6J.Cg-$Sst^{tm3.1(flpo)Zjh}$/AreckJ	Jackson Laboratory	31629
B6.129P2-$Pvalb^{tm1(cre)Arbr}$/J	Jackson Laboratory	17320
Software and algorithms		
MATLAB	Mathworks	v2021b
Suite2P v0.10.3	Pachitariu et al.[50]	https://github.com/MouseLand/suite2p
Cellpose v0.7.3	Stringer et al.[51]	https://github.com/MouseLand/cellpose
Clampex	Molecular Devices	v11
PrairieView	Bruker Nano, Inc	vX5.5
OASIS	Friedrich et al.[52]	https://github.com/j-friedrich/OASIS
Original code: Clustering Pipeline	This study	https://zenodo.org/doi/10.5281/zenodo.11371947
Original code: Code to generate manuscript figures	This study	https://zenodo.org/doi/10.5281/zenodo.11371949

EXPERIMENTAL MODEL AND STUDY PARTICIPANT DETAILS

All procedures were approved by the University of Pittsburgh Institutional Animal Care and Use Committee. Homozygous SOM-Flp mice (Cat# 31629, Jackson Laboratory, USA) were crossed with homozygous PV-Cre mice (Cat# 17320, Jackson Laboratory, USA) obtained from, and all experiments were performed in the F1 generation, which expressed Flp in SOM+ neurons and Cre in PV + neurons. Mice were group housed in cages with between 2 and 4 mice. Adult (8–24 weeks) male and female mice were used for experiments (4 male, 3 female). Mice were housed on a reversed 12 h light/dark cycle, and all experiments were performed in the dark (active) phase.

METHOD DETAILS

Surgery

12-24 h prior to surgery, mice were given a subcutaneous injection of dexamethasone (Covetrus, ME). Mice were anesthetized with isoflurane (4% for induction, 1–2% maintenance during surgery depending on breathing rate). Mice were mounted on a stereotaxic frame (David Kopf Instruments, CA). Subcutaneous injections of carprofen (Covetrus, ME) and dexamethasone were injected subcutaneously immediately prior to surgery for pain management and to reduce the inflammatory response. Ophthalmic ointment was applied to the eyes to prevent drying (Henry Schein, NY). A 4 × 4 mm craniotomy was made over PPC on the left hemisphere (centered at 2 mm posterior and 1.75 mm lateral to bregma) with a hand drill. A 1:1:2 mixture of three viruses was loaded into the glass injection pipet (1, Addgene #114471 pAAV-Ef1a-fDIO-mCherry, 2, Addgene #28306 pAAV-FLEX-tdTomato, and 3, Addgene #100837 pAAV.Syn.GCaMP6f.WPRE.SV40A). pAAV-Ef1a-fDIO mCherry was a gift from Karl Deisseroth (Addgene viral prep # 114471-AAV1; http://n2t.net/addgene:114471; RRID:Addgene_114471). pAAV-FLEX-tdTomato was a gift from Edward Boyden (Addgene viral prep # 28306-AAV1; http://n2t.net/addgene:28306; RRID:Addgene_28306). pAAV.Syn.GCaMP6f.WPRE.SV40 was a gift from Douglas Kim & GENIE Project (Addgene viral prep # 100837-AAV1; http://n2t.net/addgene:100837; RRID:Addgene_100837). A micromanipulator (QUAD, Sutter, CA) was used to target injections ~250 μm under the dura at each site, where ~60 nL virus was pressure-injected over 5–10 min. Pipets were not removed until 5 min post-injection to prevent backflow. Dental cement (Parkell, NY) sealed a glass coverslip (4 mm) over a drop of Kwik Sil (World Precision Instruments, FL) over the

craniotomy. Using dental cement, a one-sided titanium headplate was attached to the right hemisphere of the skull. After mice had recovered from the anesthesia, they were returned to their home cages, and received oral carprofen tablets (Fisher Scientific, MA) for 3 days post-surgery.

Control surgery

We performed our craniotomy surgery with the methods described above, except there were physically separated injections of the mCherry and tdTomato viral constructs at neighboring sites in each animal (six total injections). The mCherry virus was injected medially, while the tdTomato virus was injected laterally, with 1 mm separation in the mediolateral axis. The dilution of the virus was the same in all control and experimental animals, however one control animal received injections containing only the fluorophore viruses (diluted 1:10 with sterile 1X PBS) while the other received control injections that also included the GCaMP virus (2:1:1 of GCaMP/red-expressing virus/PBS).

Two-photon microscope

Images were acquired using a resonant scanning two-photon microscope (Ultima Investigator, Bruker, WI) at a 30 Hz frame rate and 512 × 512 pixel resolution through a 16× water immersion lens. PPC was imaged at a depth between 150 and 250 μm, at the level cortical layer 2/3. The angle of the objective was matched to the angle of the window. Excitation light was provided by both a tunable femtosecond infrared source (780–1100 nm) and a fixed 1045 nm wavelength laser (Insight X3, Spectra-Physics, CA). Tunable and fixed wavelength beams were combined with a dichroic mirror (ZT1040dcrb-UF3, Chroma, VT) before being routed to the microscope's galvanometers. Note that because of this optics configuration, imaging cannot be performed at tunable wavelengths immediately surrounding 1045 nm. Green and red wavelengths were separated through a 565 nm lowpass filter before passing through bandpass filters (Chroma, ET525/70 and ET 595/50, VT). PrairieView software (vX5.5 Bruker, WI) was used to control the microscope.

Behavioral monitoring

Running velocity was monitored on pitch, roll, and yaw axes using two optical sensors (ADNS- 98000, Tindie, CA) held adjacent to the spherical treadmill. A microcontroller (Teensy, 3.1, Adafruit, NY) communicated with the sensors, demixing their inputs to produce one output channel per rotational axis using custom code. Outputs controlling the galvanometers were synchronized with running velocity using a digital oscilloscope (DIGIDATA 155080, Clampex 11, Molecular Devices). Instantaneous velocity was calculated using the distance formula, using pitch and roll velocity values as inputs.

Image acquisition

Fields of view were selected based on GCaMP expression and red fluorophore expression. mCherry vs. tdTomato expression could be quickly assessed by comparing images collected at 780 nm and 1045 nm excitation, as both fluorophores were visible at 1045 nm, but only mCherry was visible at 780 nm. Multiple imaging sessions were acquired from each cranial window, varying depths and locations rostro-caudally and medio-laterally. The wavelength series to distinguish mCherry and tdTomato fluorescence was performed first. Images were collected at excitation wavelengths from 780 nm to 1100 nm in increments of 20 nm each averaged over 16 frames, excluding 1020 and 1060 nm wavelengths. The 1040 nm image was acquired with the fixed-wavelength beam from the Insight laser. At each wavelength, images were taken at multiple powers (0–275 mW). Powers were chosen for each dataset post-imaging as to avoid ones that were collected at too high or too low a power. The laser was then tuned to 920 nm for functional imaging of GCaMP fluorescence. Images were collected while mice ran voluntarily on an air-suspended spherical treadmill.[17] Functional imaging sessions were approximately 30 min in duration. All images were collected at a 30 Hz frame rate.

Image Processing

The images from the wavelength series and functional imaging were processed separately in Suite2p (v0.10.3)[50] in Python with Cellpose (v0.7.3),[51] along with 1000 frames of images collected during the functional imaging phase of the same imaging session, to allow for registration between the wavelength series and the functional imaging. Motion correction was performed on the functional images collected at 920 nm and on the wavelength series, only the functional imaging was used for ROI extraction. We then manually selected all red cells. Custom MATLAB code was used to load the two registered series of images, the wavelength series and functional imaging. Any discrepancy in registration between these two datasets was corrected by adding the peak lag of the cross correlation between the wavelength series and functional data in the X and Y directions to the coordinates of the ROIs. This correction was manually verified by plotting the circumference of the ROIs over the mean images from each image registration and confirming that the location of the ROIs relative to the cells were identical.

To further verify that each cell contained a red fluorophore, our MATLAB code was then used to plot outlines of the ROIs from the functional imaging. First, to rule out potentially ambiguous red neurons, we plotted these ROIs onto max projection of the wavelength series, as well as mean images taken from the 780-820 nm range and the 960-1045 nm range to best show mCherry or tdTomato containing cells respectively. Any ROI containing out of focus red expression or that contained overlapping red neuropil or a closely neighboring soma from another neuron was excluded from analysis entirely.

Having chosen which neurons contained red fluorophores, we generated vectors for each of the red fluorophore containing cells, where each dimension was the mean intensity of the pixels of each cell's ROI at a given wavelength. Based on our results revealing the best

wavelength combinations for separating tdTomato and mCherry from Figure 1E, we used the combination in the top 25 that has the least variability across datasets (see Figure 1E, mCherry and tdTomato ROI classification), but all combinations in the top 25 produce almost identical results after exclusion of ROIs below the silhouette score of 0.7. For our data we used the wavelengths corresponding to combination 5 in Figure 1E, consisting of the wavelengths: 780, 800, 820, 940, and 960 nm.

For the control data (Figure 1), since there was no functional data to generate ROIs in suite2p, ROIs were manually drawn. One of our two control mice had a GCaMP construct in each control injection, and there was no measured difference in clustering between control mice with and without GCaMP co-expression.

mCherry and tdTomato ROI classification

Vectors containing the mean intensity of all pixels for each ROI at each wavelength (see image processing) were run through the k-means clustering algorithm function in MATLAB. This algorithm uses a squared Euclidian distance metric for optimization and the k-means++ algorithm for cluster center initialization. Silhouette scores were calculated for each neuron using the following formula:

$$SS = \frac{distance\ to\ other\ centroid - distance\ to\ own\ centroid}{\max(distance\ own, distance\ other)}$$

The k-means clustering algorithm was applied to every possible combination of imaging wavelengths (n = 32752 combinations) described above on each of the 6 datasets from our control animals. We used the mean of the silhouette scores for all neurons in each iteration of this process as a metric of cluster separability. For all subsequent analyses, we used a specific wavelength combination that performed well across all control datasets, to maximize the stability of classification across datasets (780, 800, 820, 940, 960 nm). To determine a threshold by which cells would be excluded, we examined the distribution of silhouette scores of misclassified cells from all the iterations of clustering on control data. Note that these included 'suboptimal' combinations of wavelengths that do not distinguish mCherry and tdTomato as well. The silhouette scores from the bottom 10% of these iterations were excluded, as quantified by number of cells misclassified. This was done to remove datasets that were so noisy as to not be representative of what cluster separability would be like in intermingled data. We took two standard deviations above the mean of this distribution as a threshold for exclusion (0.7 SS). Any neuron in our experimental data that had a silhouette score lower than this value was excluded from analysis entirely. The cluster that included ROIs with strong fluorescence at 780 nm was identified as the mCherry/SOM cluster.

GCaMP fluorescence processing

Images of GCaMP fluorescence collected with 920 nm excitation were processed in a separate suite2p instance (v 0.10.3, Cellpose 0.7.3). Raw imaging movies were processed to correct for motion, identify cell bodies, and extract soma and neuropil fluorescence. Suite2p generated regions of interest (ROIs) for each cell based on anatomical features and correlations between pixels across time during functional imaging. ROIs were manually verified to be cell bodies, as opposed to dendritic processes, based on their morphology. The fluorescence of the neuropil surrounding the cell body was subtracted off from the fluorescence of the cell body, weighted by a factor of 0.7. The resulting signal was used for extracting a dF/F and deconvolved signal for each cell. ROIs classified as mCherry+ were considered SOM neurons, tdTomato+ were considered PV neurons, and GCaMP+ neurons that had no red fluorescence were considered unlabeled (UNL) neurons, pyramidal neurons comprise >90% of cortical neurons that do not express PV or SOM,[4] so UNL neurons are largely pyramidal excitatory neurons.

dF/F and deconvolution

Once the neuropil corrected fluorescence (F) timeseries was obtained for each neuron, dF/F was calculated (F-$F_{baseline}$)/$F_{baseline}$ for each frame. $F_{baseline}$ was the eighth percentile of the 900 F values surrounding that frame for a given neuron (~15 s in each direction, 30 s total). dF/F timeseries were then deconvolved to estimate the relative spike rate in each imaging frame using the OASIS toolbox.[52] We used the AR1 FOOPSI algorithm and allowed the toolbox to optimize the convolution, kernel, baseline fluorescence, and noise distribution. Deconvolved spike rates were thresholded by setting values below 0.05 to 0.

Pairwise correlations

Partial Pearson correlations were computed between all pairs of neurons for the results in Figure 2, for all combinations of cell types: UNL-UNL, SOM-SOM, PV-PV, UNL-SOM, UNL-PV, SOM-PV. Activity was boxcar smoothed in time (300 ms), and the partial Pearson correlation between the activity of the neurons was computed, discounting the effect running velocity in the pitch, roll, and yaw directions on neural activity separately (MATLAB function 'partialcorr'). This procedure was the same for Figures S5A and S5E, except pairwise correlations were only calculated on the concatenated activity of non-event periods in S5A and the concatenated activity from different events in S5E. For pairwise correlations within trials in Figure 4F, all pairwise correlations were calculated for each event, again discounting the effect of running. The effects of mean activity were discounted by subtracting the mean activity for each event before making the correlation.

Identification of PV and SOM population events

Coordinated PV, SOM, and Mixed events were identified for each imaging session as follows. The activity of individual PV and SOM neurons over the entire session was z-scored, and then neurons' activity was averaged together across cell type and box-car smoothed with a 300 ms

window. Peaks in this population activity signal were identified using MATLAB's function 'findpeaks' (MinPeakHeight: 1 standard deviation, MinPeakProminence: 2 standard deviations, MinPeakWidth: 300 ms). Peaks in interneuron population activity were considered "Mixed" if they corresponded to elevated activity in the both interneuron populations (>1/2 of the normalized activity of the population signal where the peak was identified). The onset of the events was defined by the point at which the prominence was closest to zero in the period of time defined by half of the event width prior to the first half-max (see Figure S3A for event definitions).

Event type classification

We trained linear support vector machines (SVMs) to classify whether an event was SOM or PV based on mean activity across all events at time overlapping bins spanning from 3.3 s before the onset of the event until 1.66 s after that point. Neural activity was first binned, so that each time point included the averaged activity of each neuron across the subsequent 333 ms (11 imaging frames). A distinct SVM was trained and tested on each individual time bin. Training was done on n-matched numbers of events, and performance was calculated with leave-one-out classification, based on 10-fold cross-validation, using the fitcsvm, crossval, and kfoldPredict functions in MATLAB. An identical procedure was used to classify SOM vs. PV vs. Mixed events, except a one-vs-one SVM was used. Statistical significance was calculated based on a permutation test done between 100 control classification accuracies using shuffled event type labels and our classification result for each time point.

Population vector cosine similarity

The cosine similarity between population vectors was calculated with the following formula:

$$\cos(\Theta) = \frac{A \cdot B}{\| A \| \cdot \| B \|}$$

Where Θ is the angle between the population vectors A and B, and $\cos(\Theta)$ is the cosine similarity. Population vectors were taken from the mean activity 2 s after the peak of the event. For calculating sparseness, we took the cosine similarity between each population vector and the unit vector, where each dimension had a value of 1. For calculating the cosine similarity of vectors within each event type, we took the cosine similarity between all pairwise combinations of vectors for a given event type.

Factor analysis

Factor analysis was used to measure the shared variability between neurons[53,54] using the deconvolved responses of a randomly selected subset of 75 UNL neurons within each imaging session. Factor analysis was trained on a matrix containing the deconvolved activity of all neurons at all timepoints over the event to collect 5 latent factors for SOM, PV, and Mixed events. Deconvolved activity was square root normalized to avoid biasing toward highly active neurons.[53] Training was done using 10-fold cross validation. The eigenvalue for each latent factor corresponds to the UNL population's shared variability in that dimension. This procedure was repeated 5 times for each dataset.

Histology

After all imaging sessions had been acquired, each mouse was transcardially perfused with saline and then 4% paraformaldehyde. The brain was extracted, cryoprotected, embedded, frozen, and sliced. Once slide mounted, we stained brains with DAPI to be able to identify structure. We used anatomical structure to verify the locations of our injections in PPC.

QUANTIFICATION AND STATISTICAL ANALYSIS

All pairwise comparisons across datasets were done with paired or unpaired non-parametric tests (Wilcoxon signed rank and Wilcoxon ranksum). Comparisons performed directly on deconvolved data and also on classification results were done with unpaired permutation (i.e., randomization) tests with 10,000 iterations for deconvolved, where $p < 0.0001$ indicates the highest significance for the number of runs performed. 100 iterations were performed to determine classification performance significantly better than chance from classification performed on shuffled labels. Permutation tests and non-parametric tests were run to test differences in means.